Molecular recognition using corona phase complexes made of synthetic polymers adsorbed on carbon nanotubes

Jingqing Zhang[1‡], Markita P. Landry[1‡], Paul W. Barone[1‡], Jong-Ho Kim[1,2‡] *et al.**

Understanding molecular recognition is of fundamental importance in applications such as therapeutics, chemical catalysis and sensor design. The most common recognition motifs involve biological macromolecules such as antibodies and aptamers. The key to biorecognition consists of a unique three-dimensional structure formed by a folded and constrained bioheteropolymer that creates a binding pocket, or an interface, able to recognize a specific molecule. Here, we show that synthetic heteropolymers, once constrained onto a single-walled carbon nanotube by chemical adsorption, also form a new corona phase that exhibits highly selective recognition for specific molecules. To prove the generality of this phenomenon, we report three examples of heteropolymer–nanotube recognition complexes for riboflavin, L-thyroxine and oestradiol. In each case, the recognition was predicted using a two-dimensional thermodynamic model of surface interactions in which the dissociation constants can be tuned by perturbing the chemical structure of the heteropolymer. Moreover, these complexes can be used as new types of spatiotemporal sensors based on modulation of the carbon nanotube photoemission in the near-infrared, as we show by tracking riboflavin diffusion in murine macrophages.

Molecular recognition and signal transduction are the two main challenges in sensor design[1,2]. Frequently, scientists and engineers borrow from nature to gain analyte specificity and sensitivity, using natural antibodies as vital components of the sensors[1,3–6]. However, antibodies are expensive, fragile, easily lose biological activity on external treatment (such as immobilization) and exhibit batch-dependent variation, limiting their use in widespread applications[1,6,7]. This has driven the search for methods to synthesize or discover artificial antibodies or their analogues from polymeric materials, leading to molecularly imprinted polymers[6,8] and DNA-aptamers[2,3,6].

Single-walled carbon nanotubes (SWNTs), rolled cylinders of graphene, are ideal materials for molecular recognition and signal transduction. They have near-infrared bandgap fluorescence[9] with no photobleaching threshold[10,11], and are sensitive to the surrounding environment. Electron-donating or -accepting groups can increase or decrease emission[12–14] with single-molecule sensitivity[15–17]. Adsorbates can also screen the one-dimensional confined exciton[18,19], causing solvatochromic shifts in emission[20,21], particularly with polymer wrappings that change conformation. Our laboratory and others have developed SWNT fluorescence sensors for detecting β-D-glucose[12], DNA hybridization[21], divalent metal cations[20], assorted genotoxins[22], nitroaromatics[23], nitric oxide[13,17], pH[16] and the protein avidin[14]. These efforts have invariably exploited conventional molecular recognition entities, such as enzymes[24], oligonucleotides[21] or specific functional groups with known affinity for the target molecule[13]. In this work, we instead demonstrate a new recognition motif consisting of specific polymers adsorbed onto a SWNT, whereby the interface recognizes certain small-molecule adsorbates, resulting in modulation of nanotube fluorescence (Fig. 1). We show that the recognition results from the combination of analyte adsorption to the graphene surface and lateral interactions with molecules in the adsorbed phase in a predictable manner. We introduce this concept as corona phase molecular recognition.

Screening of a polymer–SWNT library

To generate polymer–nanotube interfaces in aqueous solution, candidate amphiphilic polymers were synthesized with both hydrophobic and hydrophilic domains, enabling SWNT surface adsorption and entropic stabilization, respectively. For simplicity, only non-ionic or weakly ionic polymer phases were used in this study, to assist structural understanding. For screening, each polymer–SWNT construct was exposed to a library of 36 small molecules, and the resulting SWNT fluorescence response was monitored in triplicate using a near-infrared fluorescence spectrometer, automated to acquire data in a 96-well-plate format (Supplementary Fig. 4). Each spectrum was deconvoluted into eight SWNT chiralities using a custom spectral fitting program (Supplementary section 'Materials and Methods') that also calculates standard errors. The resulting intensity and wavelength modulations of each construct before and after the addition of each analyte in the library were recorded (for all unprocessed spectra see Supplementary Figs 23–46).

Molecular recognition by polymer corona phase on SWNTs

From the polymer–SWNT library screened to date we identified three distinct examples of polymer–nanotube-mediated molecular recognition. The simplest example is provided by a rhodamine isothiocyanate-difunctionalized poly(ethylene glycol)–SWNT complex (RITC-PEG-RITC–SWNT; Fig. 2a, 5 or 20 kDa), which exhibits fluorescence quenching exclusively in response to oestradiol (both alpha- and beta-oestradiol). Two similar synthetic variants—fluorescein isothiocyanate-difunctionalized PEG (FITC-PEG-FITC; Fig. 2b) and distearyl phosphatidylethanolamine PEG (PE-PEG; Fig. 2c)—result in non-selective response profiles. The simple polymer design allows for elucidation of the adsorbed phase structure. The selectivity of this response (Fig. 2a) is distinct from schemes using principle component analysis[22] or differential sensor responses[25] for analyte recognition, and we therefore assign

---

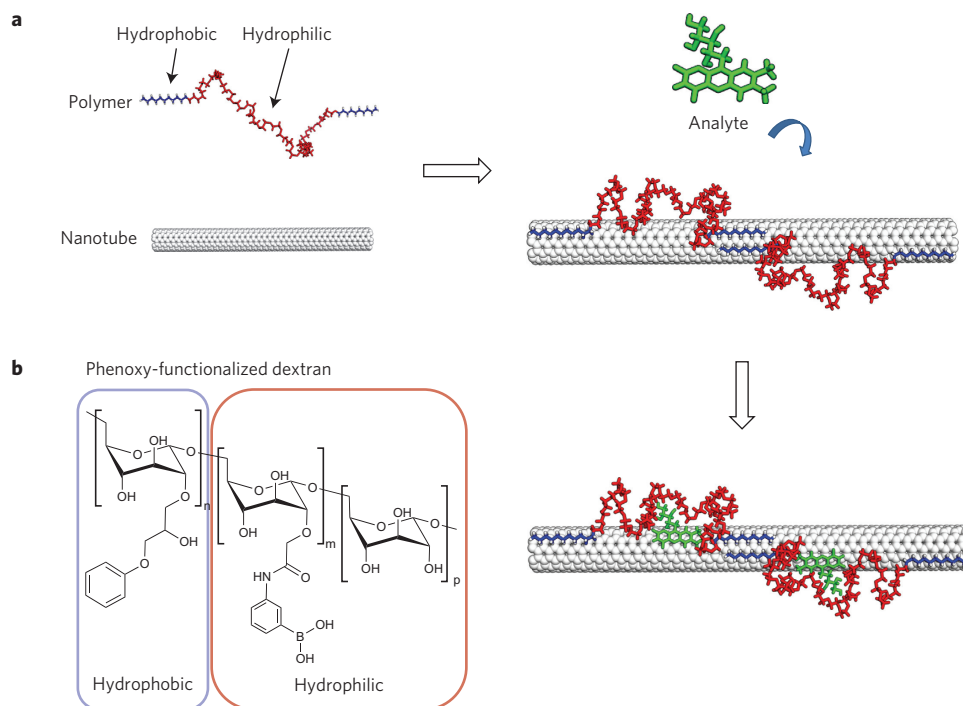*A full list of authors and their affiliations appears at the end of the paper.

Figure 1 | Schematic of the molecular recognition concept. a, A polymer with an alternating hydrophobic and hydrophilic sequence adopts a specific conformation when adsorbed to the nanotube. The polymer is pinned in place to create a selective molecular recognition site for the molecule of interest, leading to either a wavelength or intensity change in SWNT fluorescence. **b,** An example of a hydrophobic–hydrophilic alternating sequence for boronic acid-derivatized phenylated dextran.

it as the first demonstration of molecular recognition from the adsorbed phase itself. In the polymer–SWNT complex, the FITC fluorescence is quenched, providing evidence that the hydrophobic ends of the polymer are adsorbed onto the SWNT surface (Supplementary Fig. 8). The hydrophilic PEG chain is expected to form a loop extending into solution. Such a partitioning of hydrophobic and hydrophilic domains is consistent with earlier studies that have utilized PEG-conjugated hydrophobic molecules for SWNT suspension[26–32], and is supported by the experimental observation that PEG itself is incapable of suspending SWNTs. Although we do not have direct evidence of the formation of the loop structure, single-molecule fluorescent imaging of the polymer co-localized with the fluorescent SWNT is consistent and further supports both this structure and the interaction of oestradiol with the hydrophobic anchors (Supplementary Figs 9–12, Supplementary Tables 4–6).

This structural configuration is also corroborated by molecular dynamics simulations (Supplementary section 'Materials and Methods') for the three polymers (Fig. 2). Oestradiol contains an aromatic group that can adsorb to the SWNT surface if the pendant hydroxyl groups are hydrogen-bonded to the adjacent RITC amides. The molecular weight of the PEG chain does not influence the selectivity (Supplementary Figs 13–15), but the end-group structure has a substantial effect (Fig. 2a–c). The molecular recognition of the RITC-PEG-RITC–SWNT to oestradiol results from the strong interaction between the oestradiol and RITC anchors. A molecular dynamics simulation at a starting coverage of 50 polymers per 20 nm of SWNT reveals that, at equilibrium, 80% of the SWNT surface is covered by RITC anchors. We conclude that the intermolecular spacing of hydrophobic groups on the SWNT determines selectivity. Different characterization techniques have been applied here: dry-state atomic force microscopy (AFM) estimated a mean radius of 2.5 nm for RITC-PEG-RITC–SWNT, consistent with the 2.7 nm estimated from molecular dynamics

results, but smaller than the 8.1 nm that is estimated from single-particle tracking experiments (Supplementary Table 3). Under the hydrated conditions of single-particle tracking, the hydrodynamic radius can be increased. While AFM provides a direct measure of the complex radius, single-particle tracking can be influenced by the variations in nanotube length. Transmission electron microscopy (TEM) images (Supplementary Fig. 17a) indicate a range of radii from bare surface (0.47 nm) to approximately twice the AFM average value (4.9 nm), reflecting variable surface coverage along the length.

We also compared this with responses obtained from SWNTs suspended with two commonly used dispersing agents. Sodium cholate suspended SWNT (Fig. 2d) is non-responsive to the analytes tested, confirming the tight surface packing reported previously[33]. In contrast, d(GT)$_{15}$ DNA-wrapped SWNT (Fig. 3d) shows poor selectivity, suggesting a more porous interface composed of consecutive DNA helices[34]. This type of profile, which informs the accessibility of molecules to the SWNT surface, as presented in Fig. 2, allows for a unique 'fingerprinting' of polymer adsorbed phases in a manner inaccessible to other analytical techniques such as NMR, Fourier transform infrared (FTIR) spectroscopy and ultraviolet absorption. Structural schematics of the nanotube complexes were deduced from a combination of polymer molecular structure and fingerprinted response profile, further supported by single-particle tracking data and molecular dynamics results (Fig. 2).

A more complex example is provided by the PEG brush described in Fig. 3. One brush segment is alkylated for hydrophobicity while the remaining sites can display a variety of functionalities. When these sites contain Fmoc L-phenylalanine (Fmoc-Phe-PPEG8), we find that a seven-membered brush structure recognizes L-thyroxine (Fig. 3a), whereas a three-membered analogue does not (Fig. 3b). Replacing the Fmoc L-phenylalanine with amine groups also results in a loss of selectivity (NH$_2$-PPEG8, Fig. 3c) due to
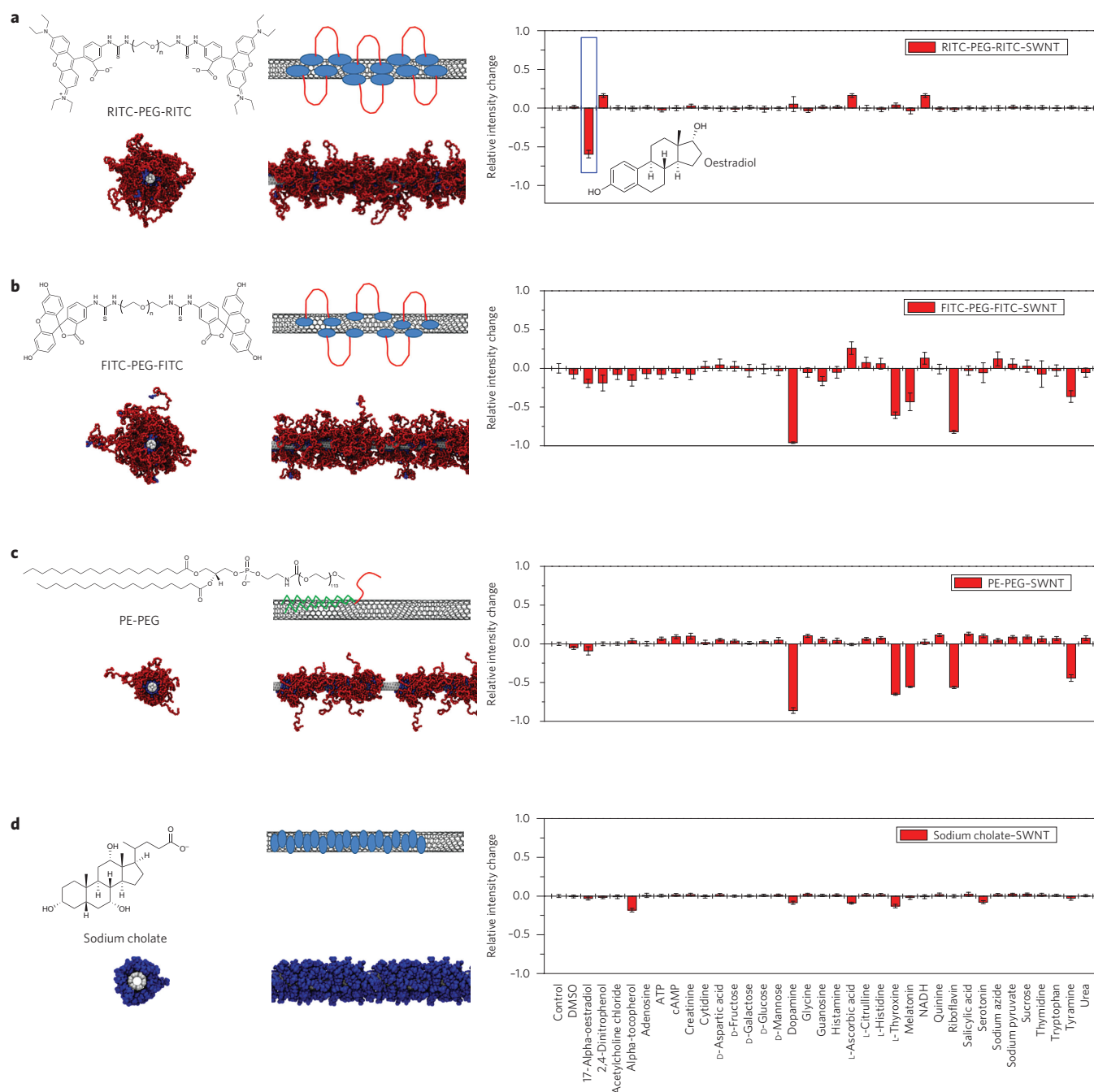
Figure 2 | Construct that selectively recognizes oestradiol, and non-selective mutants. a, RITC-PEG-RITC–SWNT enables selective recognition of oestradiol via a selective quenching response on exposure to 100 μM oestradiol. **b–d**, Chemical mutants FITC-PEG-FITC–SWNT (**b**), PE-PEG–SWNT (**c**), and sodium cholate–SWNT (**d**) lose sensitivity, selectivity, or both, to oestradiol. To the left of the bar charts are the polymer structure (top left), schematics of the polymer–SWNT complex (top right), and front (bottom left) and side (bottom right) views calculated from molecular dynamics simulations. The schematics are deduced from a combination of polymer molecular structure and fingerprinted response profile, further supported by single-particle tracking data and molecular dynamics results. Colour coding for molecular dynamics simulation results are provided in the Supplementary Information. Bar charts show intensity change of these complexes against a panel of 36 biological molecules. The error bars represent two standard deviations of triplicate measurements. Data represent (7,5) SWNT species.

the decrease in polymer hydrophobicity. For Fmoc-Phe-PPEG8–SWNT, both the aliphatic chain and the Fmoc group adsorb onto the SWNT. We propose that the strong interaction between Fmoc and L-thyroxine leads to the molecular recognition. Analogous to the previous example, we hypothesize that the PEG groups form loops, extending into the aqueous phase, imparting colloidal stability. Additionally, steric hindrance between the PEG arms influences how the Fmoc ends pack on the SWNT surface,

providing additional control of the footprint on the SWNT surface. For NH$_2$-PPEG8–SWNT, only the aliphatic chain is adsorbed on the surface of the SWNT, while the amine group, mostly protonated at pH 7.4, will extend into the aqueous phase. The less selective response profile of NH$_2$-PPEG8–SWNT suggests that the nanotube surface is more exposed compared to the Fmoc-Phe-PPEG8–SWNT and is also consistent with the polymeric structure. In addition, single-particle tracking estimates a radius of
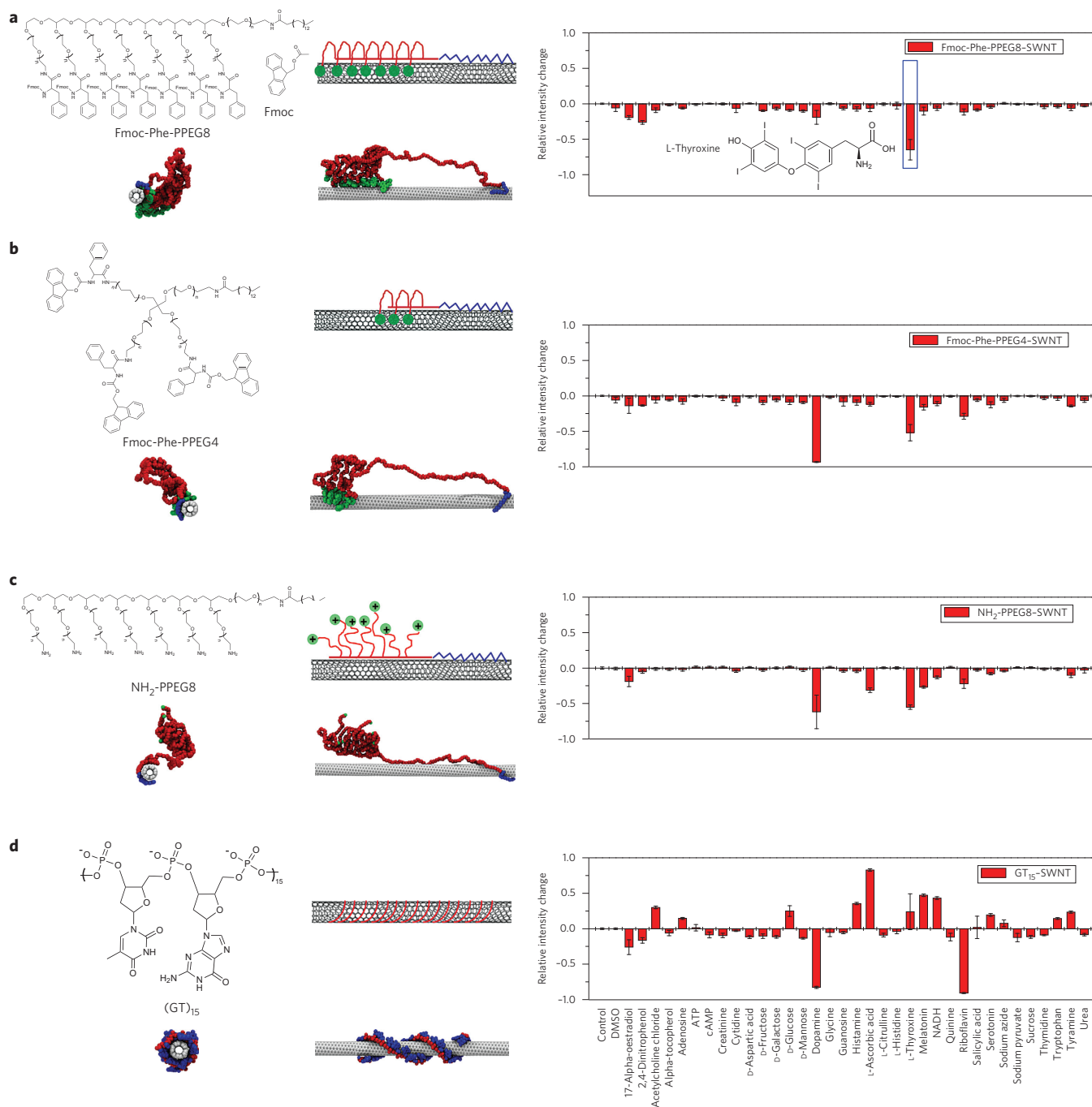
Figure 3 | Construct that selectively recognizes L-thyroxine, and non-selective mutants. a, Fmoc-Phe-PPEG8–SWNT enables selective recognition of L-thyroxine via a selective quenching response on exposure to 100 μM L-thyroxine. **b–d,** Chemical mutants Fmoc-Phe-PPEG4–SWNT (**b**), NH$_2$-PPEG–SWNT (**c**), and (GT)$_{15}$–SWNT (**d**) lose sensitivity, selectivity, or both, to L-thyroxine, as shown in the bar charts showing the intensity response of these complexes on exposure to same library of molecules. The error bars represent standard errors of triplicate measurements.

1.82 nm for the Fmoc-Phe-PPEG8–SWNT construct, consistent with the molecular dynamics estimation of 2.5 nm. However, radii estimated from TEM (Supplementary Fig. 17) and AFM (Supplementary Fig. 16) are twice as large, suggesting free polymer adsorption onto the SWNT surface during the drying process for AFM and TEM sample preparation.

Yet another example is provided by a 53 mol/mol boronic acid-substituted phenoxy-dextran-wrapped SWNT (BA-PhO-Dex–SWNT, Fig. 4). The emission maximum of the complex redshifts ~11 nm on addition of riboflavin, but not with the other diol-containing substrates that typically bind to boronic acids (Supplementary Fig. 18). The response is reversed in particular by the addition of a riboflavin-binding protein, which competitively inhibits riboflavin–SWNT binding (Supplementary Fig. 19). The optical modulation in this example is a wavelength redshift instead of fluorescence quenching as above. This type of response, attributed to solvatochromism[35] induced by a polymer dielectric change, is rare among the systems examined to date. For instance, poly(vinyl alcohol)-wrapped SWNT (PVA–SWNT, Fig. 4c) shows an intensity response to a number of analytes, including dopamine,

L-ascorbic acid, L-thyroxine, melatonin, NADH, serotonin and tyramine, but does not show any wavelength shift when screened with the molecular library. Removal of the boronic acid from the phenoxy dextran (PhO-Dex) causes a loss of selectivity, with a response from L-thyroxine (Fig. 4b). Molecular dynamics simulation shows that the introduction of the boronic acid group makes the dextran less flexible and increases the surface coverage. Meanwhile, sodium dodecyl sulphate (SDS, Fig. 4d) adsorbed SWNT shows a non-selective wavelength-shift response, presumably from a more loosely packed adsorbed layer[36,37], allowing greater molecular access to the SWNT surface. Comparison of the

radii of various polymer–SWNT complexes using multiple characterization methods is available in Supplementary Table 3 (Supplementary section 'Materials and Methods').

Equation of state model describing molecular recognition

To gain physical insight into the mechanism behind the observed polymer–analyte interactions, we developed a predictive model that can estimate analyte surface coverage θ, which is assumed to be linearly proportional to the fluorescence change $|\Delta I/I_0|$ via a constant β, or $|\Delta I/I_0| = \beta\theta$. In this work, we estimate β by choosing two reference polymers, PVA and FITC-PEG-FITC, whose combination
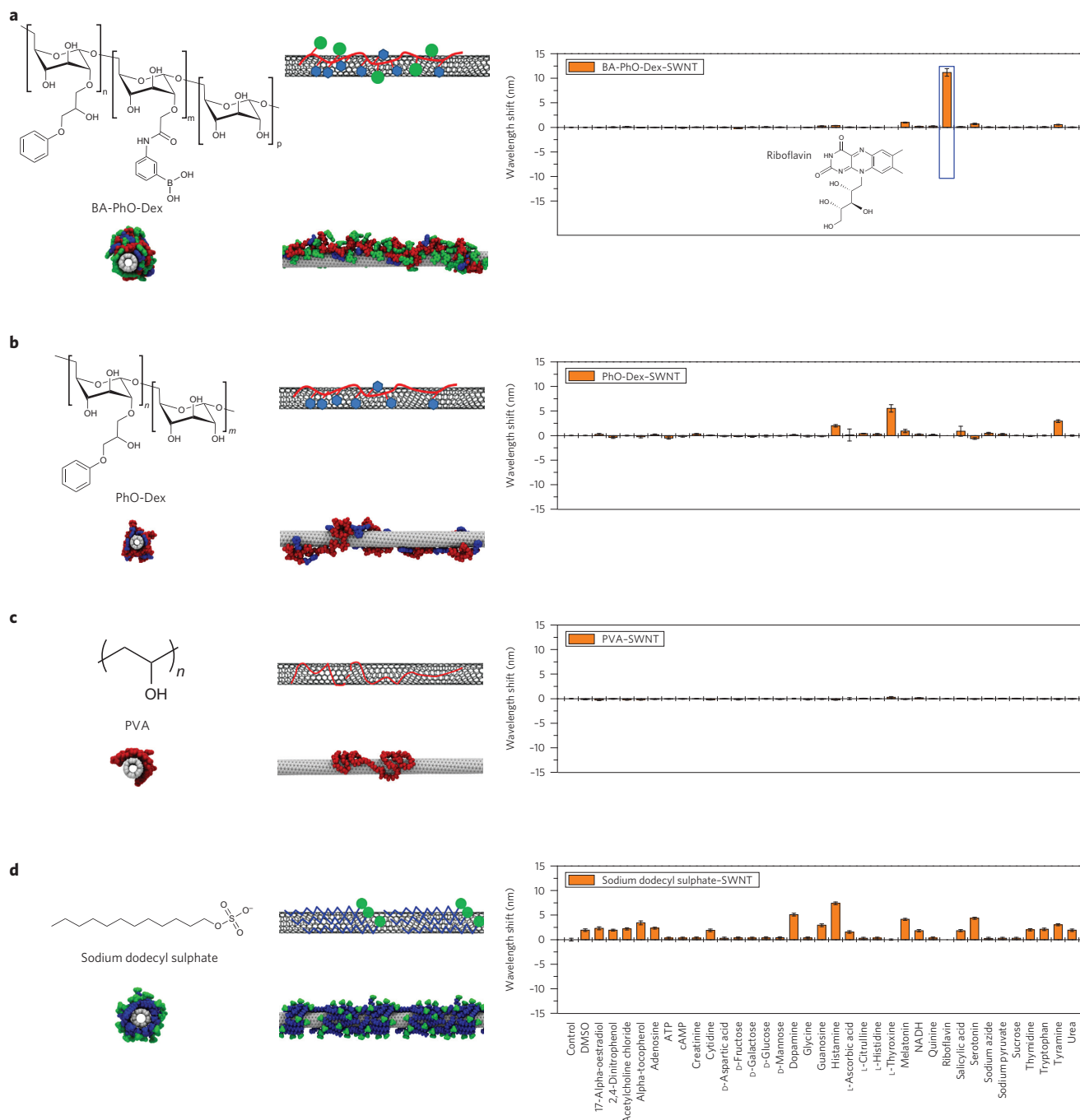

Figure 4 | Construct that selectively recognizes riboflavin, and non-selective mutants. a, BA-PhO-Dex–SWNT enables selective recognition of riboflavin via a selective wavelength shift on exposure to 100 μM riboflavin. **b–d**, Chemical mutants PhO-Dex–SWNT (**b**), PVA–SWNT (**c**), and SDS–SWNT (**d**) lose sensitivity, selectivity, or both, to riboflavin, as shown in the bar charts showing the shift in emission wavelength of SWNT complexes against the same library of molecules. The error bars represent two standard deviations of triplicate measurements. Data represent (7,6) SWNT species.
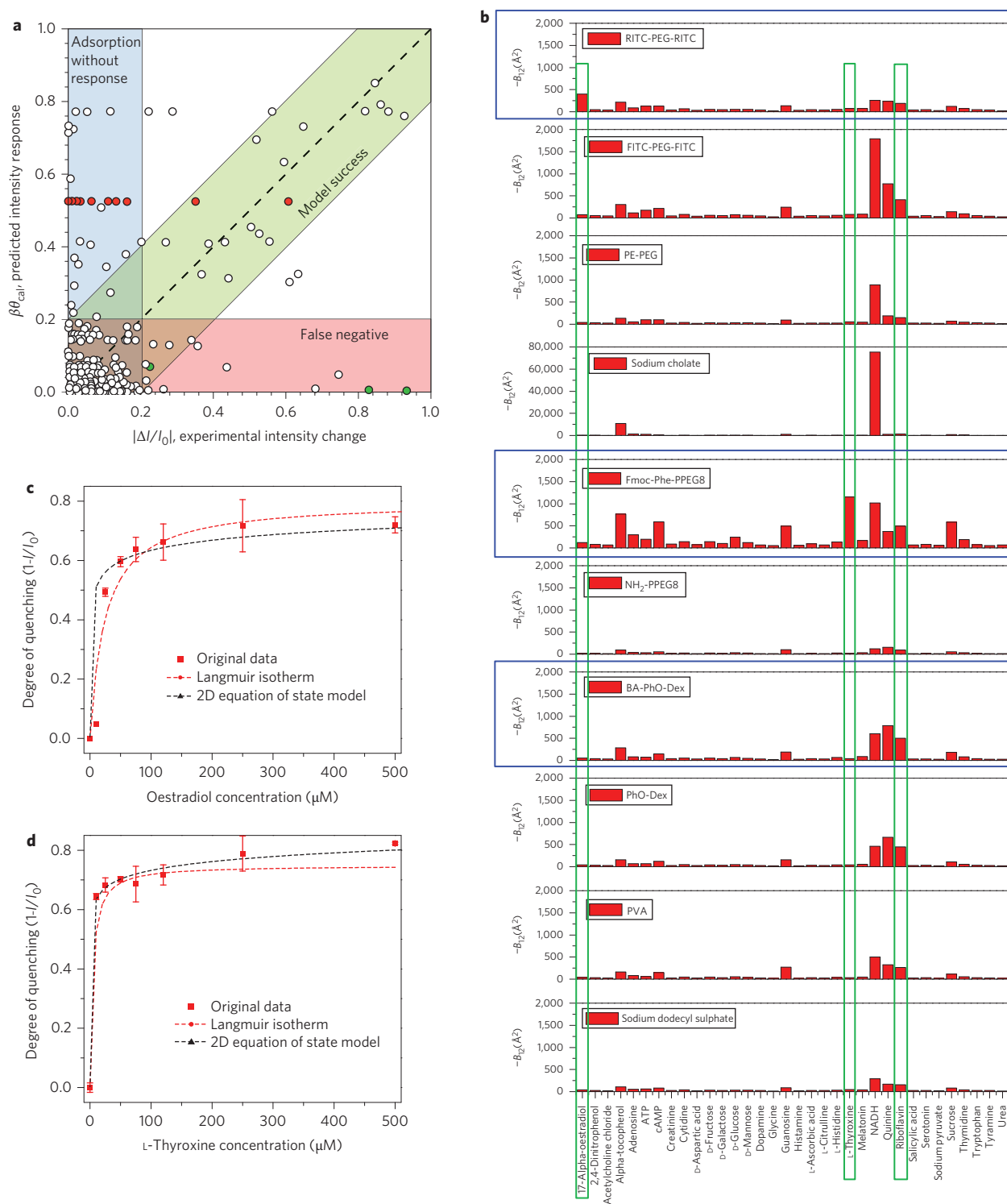
Figure 5 | Two-dimensional equation of state model for describing molecular recognition. a, Calculated intensity response, $\beta\theta_{cal}$, as a function of experimental intensity modulation, which is the absolute value of $\Delta I/I_0$. Green region: modelled responses are within 20% error of the actual responses, which accounts for 83% of all data. Blue is the 'false-positive' region (13.1%), where the model over-predicts the response more than 20%. Pink is the region (3.7%) where the model under-predicts the response by more than 20%. Over-predicted NADH responses are shown as red dots and under-predicted dopamine responses as green dots. **b**, B_{12} values for each pair of analyte and polymer anchor. Blue and green boxes highlight the molecular recognition cases. **c**, Fluorescence quenching of (7,5) RITC-PEG-RITC–SWNT as a function of oestradiol concentration. Dashed red lines are fits of the data to a Type I Langmuir adsorption isotherm with $K_d = 25\ \mu M$ and $|\Delta I/I|_{max} = 0.80$. Dashed black lines are fits of the data to the two-dimensional equation of state model with $\beta = 1$ and $B_{12} = -400\ Å^2$. **d**, Fluorescence quenching of (7,5) Fmoc-Phe-PPEG8–SWNT as a function of L-thyroxine concentration. Dashed red lines are fits of the data to a Type I Langmuir adsorption isotherm, with $K_d = 2.3\ \mu M$ and $|\Delta I/I|_{max} = 0.76$. Dashed black lines are fits of the data to the two-dimensional equation of state model with $\beta = 3.2$ and $B_{12} = -1,150\ Å^2$. Data were taken with three replicates, and error bars are two standard deviations.
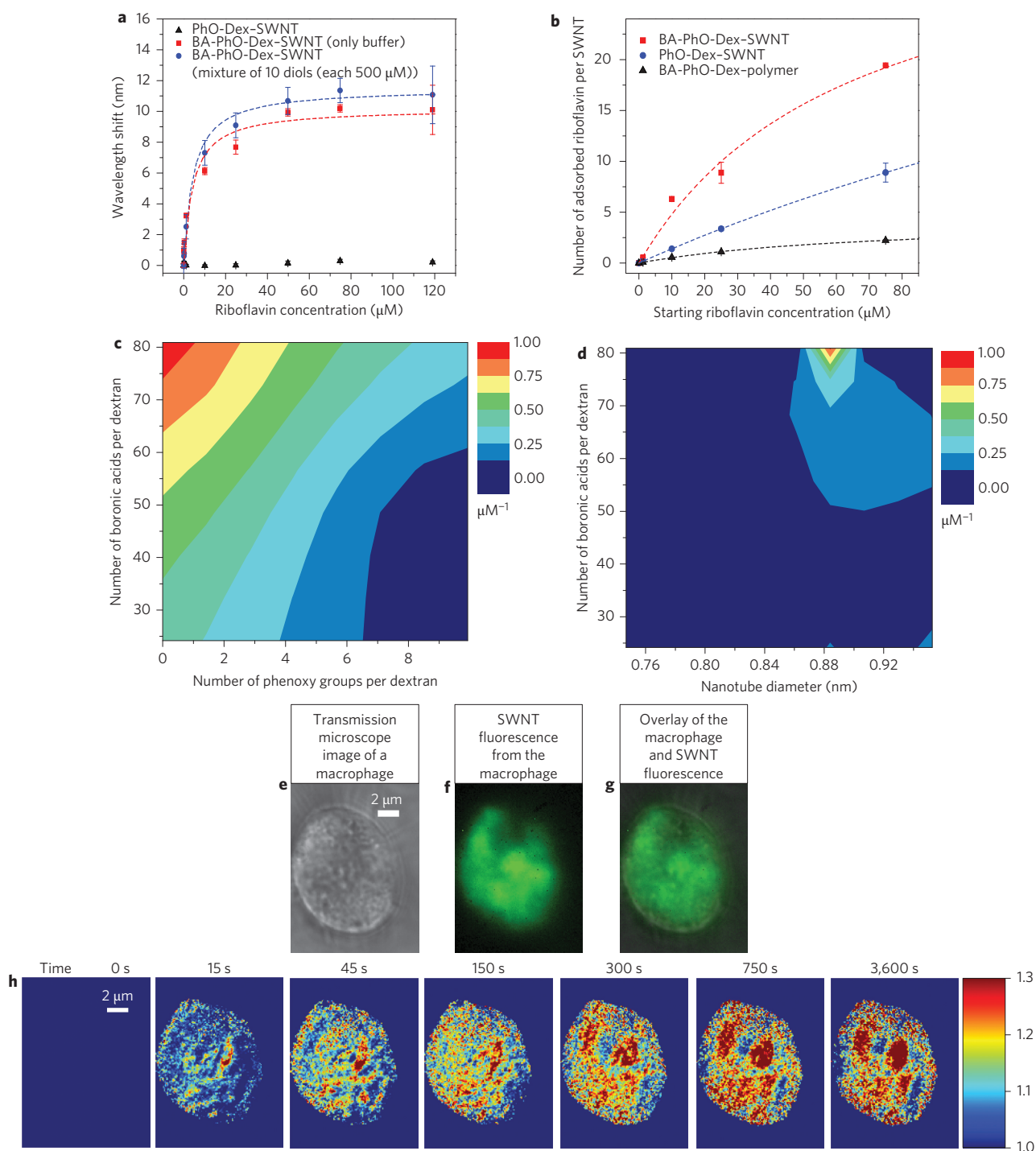
Figure 6 | Tunability of BA-PhO-Dex–SWNT sensor, and application in spatial and temporal chemical imaging in live Raw 264.7 macrophage cells.
a, Shift in emission maximum of a (7,6) nanotube as a function of riboflavin concentration for BA-PhO-Dex–SWNTs (red squares) and PhO-Dex–SWNTs (black triangles). A competitive binding curve (blue circles) is also shown for BA-PhO-Dex–SWNT, where each concentration of riboflavin is also mixed with ten additional diol-containing molecules . Dashed lines are fits of the data with a Type I Langmuir adsorption isotherm with $K_d = 4.23$ μM and $\Delta\lambda_{max} = 10.2$ nm, and with $K_d = 4.39$ μM and $\Delta\lambda_{max} = 11.5$ nm without the competing analyte. The PhO-Dex–SWNT shifting response could not be fit to a Type I isotherm. Reported data points are averages of three separate measurements and reported error bars are two standard deviations. **b**, Number of adsorbed riboflavin per SWNT as a function of starting riboflavin concentration, measured by radiolabelling experiments. Fitting the data with a Type I Langmuir isotherm reveals $K_d = 64.2, 344, 72.4$ μM and $\Delta\theta_{max} = 36, 50, 4.4$ riboflavin per SWNT for BA-PhO-Dex–SWNT, PhO-Dex–SWNT and BA-PhO-Dex–polymer, respectively. For the case of the polymer, the experiments were performed such that an equal amount of unbound BA-PhO-Dex polymer as BA-PhO-Dex–SWNT solution was used. **c**, Contour plot of $1/K_d$ for the (7,6) nanotube plotted versus polymer composition. **d**, Contour plot of $1/K_d$ plotted as a function of nanotube diameter versus boronic acid content. **e–g**, Brightfield image of a macrophage RAW 264.7 (**e**), near-infrared fluorescence of BA-PhO-Dex–SWNTs inside the macrophage before the addition of riboflavin (**f**), and the resultant overlay (**g**). **h**, Time evolution of the fluorescence from cell-encapsulated BA-PhO-Dex–SWNTs in response to extracellular riboflavin added at time $t = 36$ s. The emission maximum shifting response is represented by the normalized intensity of the right channel (longer wavelength) divided by the normalized intensity of the left channel (shorter wavelength).

provides a relatively complete fluorescence response profile for all the analytes tested such that

$$\overline{\beta}_{PVA.FITC-PEG-FITC}$$
$$\equiv \frac{\beta_{PVA}(|\Delta I/I_0|)_{PVA} + \beta_{FITC-PEG-FITC}(|\Delta I/I_0|)_{FITC-PEG-FITC}}{(|\Delta I/I_0|)_{PVA} + (|\Delta I/I_0|)_{FITC-PEG-FITC}}$$

Competitive adsorption of the analyte molecule and polymer anchors on the SWNT surface can be described using a variation of a thermodynamic model for surfactant partitioning at the air–water interface[38]. The equation of state is given by

$$\ln(x_{li}) = \frac{\Delta\mu_i^0}{k_B T} + \ln\left(\frac{x_i^s}{a - \sum_k x_k^s a_k}\right) + \frac{a_i + 2\pi r_i \sum_k x_k^s r_k}{a - \sum_k x_k^s a_k} \qquad (1)$$
$$+ \frac{\pi a_i (\sum_k x_k^s r_k)^2}{(a - \sum_k x_k^s a_k)^2} + \frac{2}{a} \sum_k B_{ik} x_k^s$$

where x_i^s represents the molar fraction of species i on the surface, a is the area occupied per adsorbed surfactant molecule, and $\Delta\mu_i^0$ defines the standard-state chemical potential difference at the surface and in the bulk. Adsorbing molecules are modelled as adsorbing hard discs with molecular radius r_i and area a_i, in equilibrium with a bulk monomer with mole fraction x_{li}. We designate species 1 as the polymer anchor and species 2 as the analyte. B_{11} and B_{22} describe the self-interaction of the molecules, whereas B_{12} (and equivalently B_{21}) describes interactions between the analyte and polymer anchors.

For each pair of polymer and analyte, the thermodynamic parameters (B_{11}, B_{12}, B_{22}, $\Delta\mu_1^0$, $\Delta\mu_2^0$) can be estimated a priori with molecular simulations, and (x_1^s, x_2^s, a) are then solved using equation (1). The calculated surface coverage is estimated using $\theta_{cal} = a_2 x_2^s/a$ and together with $\overline{\beta}_{PVA,FITC-PEG-FITC}$ gives the calculated $|\Delta I/I_0|$ for the (analyte, anchor) pairs for the other nine polymers, to be compared with the experimental $|\Delta I/I_0|$ in Fig. 5a. $\overline{\beta}_{PVA,FITC-PEG-FITC}$ is used to approximate β, which is considered to be only analyte-dependent. Therefore, after evaluating this parameter once, the same value can subsequently be used for all future polymer–SWNT constructs as long as the same library of analytes is used for screening.

Using this model, 83% of fluorescence responses are predicted within 20% error of their experimental values (green in Fig. 5a), successfully describing all three polymer recognition cases described in this work. The restrictive assumptions, however, do not allow for accurate modelling of NADH and dopamine. For NADH (red circles in Fig. 5a), the model over-predicts the response, while dopamine (green circles), among others, falls into the false-negative region, contributing to a 3.7% false-negative rate in Fig. 5a. The B_{12} values (Fig. 5b) suggest that the primary mechanism of selectivity is a favourable interaction between the analyte and the adsorbed polymer anchors. For example, oestradiol has the highest B_{12} value (400 Å²) among analytes for RITC-PEG-RITC. The same is true for L-thyroxine (1,150 Å²) on Fmoc-Phe-PPEG8, where the oestradiol interaction falls to 122 Å². In the case of riboflavin (500 Å²) on BA-PhO-Dex, the pattern also holds, with negligible values for oestradiol (54 Å²) and L-thyroxine (41 Å²). Future work will address analyte–anchor interactions allowing for conformational changes at the graphene surface.

This formalism can also describe the adsorption isotherms of oestradiol responding to RITC-PEG-RITC–SWNT and thyroxine responding to Fmoc-Phe-PPEG8–SWNT, if B_{12} and β are instead treated as adjustable parameters (Fig. 5c,d, black dashed lines). It therefore provides a theoretical basis for designing selective polymer–SWNT constructs for molecules of

interest. It is instructive to compare the apparent dissociation constants K_d, in each case, which span a range of values and are diminished with chemical modification of the polymer phase. The response, either $|\Delta I/I_0|$ or $|\Delta\lambda|$, can be described by a Type I adsorption isotherm, or $\Delta\lambda = \Delta\lambda_{max} C/(C + K_d)$ (Figs 5c,3d,4a). We find K_d to be 25 µM for RITC-PEG-RITC–SWNT to oestradiol, 2.3 µM for Fmoc-Phe-PPEG8–SWNT to L-thyroxine, and 4.2 µM for BA-PhO-Dex–SWNT to riboflavin. The selectivity and binding affinity of BA-PhO-Dex–SWNT to riboflavin is unaffected by the presence of a mixture of ten competing diols, demonstrating the practical utility of the sensor (Fig. 6a, blue). Radiolabelling of riboflavin with ³H (Fig. 6b) reveals partitioning of riboflavin into the polymer corona of the non-selective PhO-Dex–SWNT ($K_d = 344$ µM, $\theta_{max} = 50$ riboflavin per SWNT), but the affinity is 5.3 times lower than the selective construct ($K_d = 64.2$ µM, $\theta_{max} = 36$ riboflavin per SWNT). In addition, an equal amount of unbound BA-PhO-Dex polymer as in the BA-PhO-Dex–SWNT solution shows $K_d = 72.4$ µM, $\theta_{max} = 4.4$ riboflavin per SWNT, demonstrating minimal binding sites on just the polymer alone. It is likely that the K_d in this case appears larger than that measured from SWNT fluorescence because unbound riboflavin is removed before measuring radioactivity, potentially offsetting the binding equilibrium.

Tunable analyte binding constant
The structure of the BA-PhO-Dex–SWNT allows exploration of the influence of small changes in polymer composition on the binding constant. Dextran alone does not suspend SWNTs, and the phenoxy groups create SWNT attachment sites via π-stacking[39,40]. One can alter the polymer composition in a manner analogous to allosteric mutagenesis in proteins[41,42] and examine the resulting K_d of each variant. The K_d for riboflavin decreases with increasing boronic acid:dextran ratio and decreasing phenoxy:dextran ratio (Fig. 6c), with optimal binding occurring at an SWNT diameter of 0.88 nm (Fig. 6d). K_d can be decreased 1,600-fold to 1.03 µM (Supplementary Table 2) by selecting a polymer composition of 80 mol/mol boronic acid:dextran and the (7,6) chirality nanotube. This K_d is similar to analyte binding proteins such as glucose binding protein[43] ($K_d = 0.4$ µM). Hence, the binding affinity of these SWNT complexes is comparable to some naturally occurring proteins and biorecognition sites.

Tracking riboflavin diffusion in macrophage cells
The recognition sites created in this work have immediate utility as fluorescent sensors of biological molecules. To demonstrate this, we utilized the BA-PhO-Dex–SWNT construct as an intracellular riboflavin sensor. Riboflavin is an essential vitamin for eukaryotic organisms and its transport is typically facilitated by riboflavin carrier protein[44], for which elevated levels may predict late-stage (stage III or IV) breast cancer with 100% accuracy[45]. We incubated BA-PhO-Dex–SWNT with Raw 264.7 macrophage cells in a riboflavin-free medium[13] overnight (Fig. 6e–g). Using a home-built near-infrared, dual-channel imaging microscope[23], we spatially imaged the wavelength shifts of the (7,6) SWNT, $\lambda_{max} = 1,147$ nm, on riboflavin binding within murine macrophages cultured in riboflavin-free media (Supplementary Fig. 20). On addition of riboflavin to the extracellular media, the fluorescence of SWNTs inside the cell redshifts systematically over time (Fig. 6h), responding to the diffusion of riboflavin into the cell (Supplementary Movie 1). This is a demonstration of dynamic, high-resolution detection of intracellular riboflavin concentration gradients.

Conclusions
We have reported a new and generic molecular recognition concept, called corona phase molecular recognition, arising from a folded and constrained heteropolymer pinned at an SWNT interface via

surface forces. The recognition is realized only once the polymer and the SWNT are conjugated with each other, while the polymers by themselves have little to no previously identified connection or affinity for the analytes of interest. We designate this effect 'corona phase' molecular recognition to highlight the essential role of both the polymer and nanotube surfaces, and we note that comparable spherical and elliptical nanoparticles may also show phases capable of molecular recognition. The observation that binding sites formed in this manner have tunable affinity following small changes in polymer composition and nanotube chirality indicates that the potential parameter space is exceedingly large. Furthermore, a theoretical framework based on a two-dimensional equation of state provides a quantitative understanding of the library of responses and offers strong mechanistic insight for the recognition. Our work provides a platform that can be used in various fields, such as sensor development, nanoparticle surface science, single-molecule polymer physics and the study of nanoparticle–biomolecule interactions. However, of immediate utility are the families of fluorescent constructs that can be used for real-time, intracellular detection of important biomolecules, as demonstrated experimentally in this work.

References

1. Saerens, D., Huang, L., Bonroy, K. & Muyldermans, S. Antibody fragments as probe in biosensor development. *Sensors* **8**, 4669–4686 (2008).
2. Cho, E. J., Lee, J. W. & Ellington, A. D. Applications of aptamers as sensors. *Annu. Rev. Anal. Chem.* **2**, 241–264 (2009).
3. Ellington, A. D. & Szostak, J. W. *In vitro* selection of RNA molecules that bind specific ligands. *Nature* **346**, 818–822 (1991).
4. Byrne, B., Stack, E., Gilmartin, N. & O'Kennedy, R. Antibody-based sensors: principles, problems and potential for detection of pathogens and associated toxins. *Sensors* **9**, 4407–4445 (2009).
5. De Koning-Ward, T. F. *et al.* A newly discovered protein export machine in malaria parasites. *Nature* **459**, 945–949 (2009).
6. Skottrup, P. D., Nicolaisen, M. & Justesen, A. F. Towards on-site pathogen detection using antibody-based sensors. *Biosens. Bioelectron.* **24**, 339–348 (2008).
7. Peluso, P. *et al.* Optimizing antibody immobilization strategies for the construction of protein microarrays. *Anal. Biochem.* **312**, 113–124 (2003).
8. Turner, A. P. F. & Piletsky, S. Biosensors and biomimetic sensors for the detection of drugs, toxins and biological agents. *Nato Sec. Sci. B Phys.* **1**, 261 (2005).
9. O'Connell, M. J. *et al.* Band gap fluorescence from individual single-walled carbon nanotubes. *Science* **297**, 593–596 (2002).
10. Li, Q. *et al.* Sustained growth of ultralong carbon nanotube arrays for fiber spinning. *Adv. Mater.* **18**, 3160–3163 (2006).
11. Heller, D. A., Baik, S., Eurell, T. E. & Strano, M. S. Single-walled carbon nanotube spectroscopy in live cells: towards long-term labels and optical sensors. *Adv. Mater.* **17**, 2793–2798 (2005).
12. Barone, P. W., Baik, S., Heller, D. A. & Strano, M. S. Near-infrared optical sensors based on single-walled carbon nanotubes. *Nature Mater.* **4**, 86–92 (2005).
13. Kim, J. *et al.* The rational design of nitric oxide selectivity in single-walled carbon nanotube near-infrared fluorescence sensors for biological detection. *Nature Chem.* **1**, 473–481 (2009).
14. Satishkumar, B. C. *et al.* Reversible fluorescence quenching in carbon nanotubes for biomolecular sensing. *Nature Nanotech.* **2**, 560–564 (2007).
15. Jin, H., Heller, D. A., Kim, J. & Strano, M. Stochastic analysis of stepwise fluorescence quenching reactions on single-walled carbon nanotubes: single molecule sensors. *Nano Lett.* **8**, 4299–4304 (2008).
16. Cognet, L. Stepwise quenching of exciton fluorescence in carbon nanotubes by single-molecule reactions. *Science* **316**, 1465 (2007).
17. Zhang, J. *et al.* Single molecule detection of nitric oxide enabled by d(AT)$_{15}$ DNA adsorbed to near infrared fluorescent single-walled carbon nanotubes. *J. Am. Chem. Soc.* **133**, 567–581 (2010).
18. Perebeinos, V., Tersoff, J. & Avouris, P. Scaling of excitons in carbon nanotubes. *Phys. Rev. Lett.* **92**, 257402 (2004).
19. Walsh, A. G. *et al.* Screening of excitons in single, suspended carbon nanotubes. *Nano Lett.* **7**, 1485–1488 (2007).
20. Heller, D. A. *et al.* Optical detection of DNA conformational polymorphism on single-walled carbon nanotubes. *Science* **311**, 508–511 (2006).
21. Jeng, E. S., Moll, A. E., Roy, A. C., Gastala, J. B. & Strano, M. S. Detection of DNA hybridization using the near-infrared band-gap fluorescence of single-walled carbon nanotubes. *Nano Lett.* **6**, 371–375 (2006).
22. Heller, D. A. *et al.* Multimodal optical sensing and analyte specificity using single-walled carbon nanotubes. *Nature Nanotech.* **4**, 114–120 (2008).
23. Heller, D. A. *et al.* Peptide secondary structure modulates single-walled carbon nanotube fluorescence as a chaperone sensor for nitroaromatics. *Proc. Natl Acad. Sci. USA* **108**, 8544–8549 (2011).
24. Barone, P. W., Parker, R. S. & Strano, M. S. *In vivo* fluorescence detection of glucose using a single-walled carbon nanotube optical sensor: design, fluorophore properties, advantages, and disadvantages. *Anal. Chem.* **77**, 7556–7562 (2005).
25. Gruber, K. *et al.* Cantilever array sensors detect specific carbohydrate–protein interactions with picomolar sensitivity. *ACS Nano* **5**, 3670–3678 (2011).
26. Robinson, J. *et al.* High performance *in vivo* near-IR (>1 μm) imaging and photothermal cancer therapy with carbon nanotubes. *Nano Res.* **3**, 779–793 (2010).
27. Robinson, J. T. *et al.* *In vivo* fluorescence imaging in the second near-infrared window with long circulating carbon nanotubes capable of ultrahigh tumor uptake. *J. Am. Chem. Soc.* **134**, 10664–10669 (2012).
28. Kosuge, H. *et al.* Near infrared imaging and photothermal ablation of vascular inflammation using single-walled carbon nanotubes. *J. Am. Heart Assoc.* **1**, 1–9 (2012).
29. Prencipe, G. *et al.* PEG branched polymer for functionalization of nanomaterials with ultralong blood circulation. *J. Am. Chem. Soc.* **131**, 4783–4787 (2009).
30. Chen, Z. *et al.* Protein microarrays with carbon nanotubes as multicolor Raman labels. *Nature Biotechnol.* **26**, 1285–1292 (2008).
31. Welsher, K. *et al.* A route to brightly fluorescent carbon nanotubes for near-infrared imaging in mice. *Nature Nanotech.* **4**, 773–780 (2009).
32. Nakayama-Ratchford, N., Bangsaruntip, S., Sun, X., Welsher, K. & Dai, H. Noncovalent functionalization of carbon nanotubes by fluorescein–polyethylene glycol: supramolecular conjugates with pH-dependent absorbance and fluorescence. *J. Am. Chem. Soc.* **129**, 2448–2449 (2007).
33. Lin, S. & Blankschtein, D. Role of the bile salt surfactant sodium cholate in enhancing the aqueous dispersion stability of single-walled carbon nanotubes: a molecular dynamics simulation study. *J. Phys. Chem. B* **114**, 15616–15625 (2010).
34. Zheng, M. *et al.* Structure-based carbon nanotube sorting by sequence-dependent DNA assembly. *Science* **302**, 1545–1548 (2003).
35. Choi, J. H. & Strano, M. S. Solvatochromism in single-walled carbon nanotubes. *Appl. Phys. Lett.* **90**, 223114 (2007).
36. Tummala, N. R. & Striolo, A. SDS surfactants on carbon nanotubes: aggregate morphology. *ACS Nano* **3**, 595–602 (2009).
37. Xu, Z., Yang, X. & Yang, Z. A molecular simulation probing of structure and interaction for supramolecular sodium dodecyl sulfate/single-wall carbon nanotube assemblies. *Nano Lett.* **10**, 985–991 (2010).
38. Mulqueen, M. & Blankschtein, D. Prediction of equilibrium surface tension and surface adsorption of aqueous surfactant mixtures containing ionic surfactants. *Langmuir* **15**, 8832–8848 (1999).
39. Zorbas, V. *et al.* Preparation and characterization of individual peptide-wrapped single-walled carbon nanotubes. *J. Am. Chem. Soc.* **126**, 7222–7227 (2004).
40. Zheng, M. *et al.* DNA-assisted dispersion and separation of carbon nanotubes. *Nature Mater.* **2**, 338–342 (2003).
41. Scrutton, N. S., Berry, A. & Perham, R. N. Redesign of the coenzyme specificity of a dehydrogenase by protein engineering. *Nature* **343**, 38–43 (1990).
42. Lindberg, R. L. P. & Negishi, M. Alteration of mouse cytochrome P$_{450}$coh substrate specificity by mutation of a single amino-acid residue. *Nature* **339**, 632–634 (1989).
43. Ge, X., Tolosa, L. & Rao, G. Dual-labeled glucose binding protein for ratiometric measurements of glucose. *Anal. Chem.* **76**, 1403–1410 (2004).
44. Mason, C. W. *et al.* Recognition, cointernalization, and recycling of an avian riboflavin carrier protein in human placental trophoblasts. *J. Pharmacol. Exp. Ther.* **317**, 465–472 (2006).
45. Rao, P. N. *et al.* Elevation of serum riboflavin carrier protein in breast cancer. *Cancer Epidemiol. Biomark. Prev.* **8**, 985–990 (1999).

Author contributions

M.S.S. conceived and developed the recognition concept, with input from P.W.B. and D.A.H. Authors J.Z., M.P.L., P.W.B. and J.K. contributed equally to this work. J.Z., P.W.B. and M.S.S. analysed the data and co-wrote the manuscript, with contributions from S.B.

and M.P.L. J.Z., P.W.B. and J.K. synthesized various polymers, suspended SWNTs with them, conducted the high-throughput screening assay and additional experiments, with contributions from A.R., A.C.H., M.A.S., K.Y. and J.A. J.Z. and A.J.H. performed the radiolabelling experiment and collaborated with R.G.C., D.Li and J.M.E. on the experimental protocol. J.Z. performed the *in vitro* cell experiments for riboflavin detection and processed images generated from the dual-channel microscope with D.Lin. M.P.L. built the near-infrared/visible dual-channel total-internal reflection fluorescence microscope and processed the generated images. A.J.H. contributed to the automation of single-molecule image analysis. S.L. and D.B. conducted molecular dynamics simulation and analysed the results. M.S.S. and D.B. conceived and designed the two-dimensional equation of state model with Z.W.U. and J.Z., while Z.W.U. performed the necessary molecular simulations. B.M. and J.Z. worked on polymer–SWNT complex characterization. S.K. performed additional TEM experiments. M.S.S. and D.A.H. conceived, designed and built the dual-channel microscope and performed additional analyte screening. J.Z. and D.Lin developed the imaging-processing algorithm for the images generated during the dual-channel microscope experiment. A.A.B. and H.J. developed the single-particle tracking algorithm. F.S., S.S. and M.P.L. conducted additional single-molecule experiments and performed data analysis. P.W.B. and N.N. developed the automated spectrum deconvolution program, which was further improved by J.Z. and A.J.H.

Additional information

Competing financial interests

The authors declare no competing financial interests.

Jingqing Zhang[1‡], Markita P. Landry[1‡], Paul W. Barone[1‡], Jong-Ho Kim[1,2‡], Shangchao Lin[1,3], Zachary W. Ulissi[1], Dahua Lin[4], Bin Mu[1], Ardemis A. Boghossian[1], Andrew J. Hilmer[1], Alina Rwei[1], Allison C. Hinckley[1], Sebastian Kruss[1], Mia A. Shandell[5†], Nitish Nair[1†], Steven Blake[1], Fatih Şen[1,6], Selda Şen[1,7], Robert G. Croy[5,8], Deyu Li[5,8], Kyungsuk Yum[1†], Jin-Ho Ahn[1†], Hong Jin[1†], Daniel A. Heller[1,9], John M. Essigmann[5,8], Daniel Blankschtein[1] and Michael S. Strano[1*]

[1]Department of Chemical Engineering, Massachusetts Institute of Technology, Cambridge, Massachusetts 02139, USA, [2]Department of Chemical Engineering, Hanyang University, Ansan 426-791, Republic of Korea, [3]Department of Mechanical Engineering, Massachusetts Institute of Technology, Cambridge, Massachusetts 02139, USA, [4]Department of Electrical Engineering and Computer Science, Massachusetts Institute of Technology, Cambridge, Massachusetts 02139, USA, [5]Department of Chemistry, Massachusetts Institute of Technology, Cambridge, Massachusetts 02139, USA, [6]Department of Chemistry, Dumlupinar University, Kutahya 43020, Turkey, [7]Department of Chemistry, Middle East Technical University, Ankara 06531, Turkey, [8]Department of Biological Engineering, Massachusetts Institute of Technology, Cambridge, Massachusetts 02139, USA, [9]Molecular Pharmacology and Chemistry Program, Memorial Sloan-Kettering Cancer Center, New York, New York 10065, USA, [†]Present address: Department of Pharmacology, Graduate School of Arts & Sciences at Columbia University Medical Center, 630 West 168th Street, PH 7W 318, New York, New York 10032, USA (M.A.S.), Computational Centre of Expertise, Shell India Markets Private Limited, Bangalore, India 560 048 (N.N.), Samsung Advanced Institute of Technology, Samsung Electronics Co, Yongin-Si, Gyeonggi-Do, Korea 446-712 (J-H.A.), Department of Materials Science and Engineering, University of Texas at Arlington, 501 West First Street, Arlington, Texas 76019, USA (K.Y.), National Institute of Clean-and-Low-Carbon Energy (NICE), PO Box 001 Shenhua NICE, Future Science and Technology City, Changping District, Beijing 102209, China (H.J.), [‡]These authors contributed equally to this work. *e-mail: strano@mit.edu